PHYSICAL REVIEW D **84,** 054503 (2011)

Coupled channel analysis of the ρ meson decay in lattice QCD

C. B. Lang,[1,*] Daniel Mohler,[2,†] Sasa Prelovsek,[3,4,‡] and Matija Vidmar[4]

[1]*Institut für Physik, FB Theoretische Physik, Universität Graz, A–8010 Graz, Austria*
[2]*TRIUMF, 4004 Wesbrook Mall, Vancouver, British Columbia V6T 2A3, Canada*
[3]*Department of Physics, University of Ljubljana, Slovenia*
[4]*Jozef Stefan Institute, Ljubljana, Slovenia*

(Received 30 May 2011; published 9 September 2011)

We employ a variational basis with a number of $\bar{q}q$ and $\pi\pi$ lattice interpolating fields with quantum numbers of the ρ resonance to extract the discrete energy spectrum in a finite volume. In the elastic region, this spectrum is related to the phase shift of the continuum scattering amplitude by Lüscher's formula, and the relation allows the extraction of resonance parameters from the spectrum calculation. The simulations are performed at three different total momenta of the coupled $\bar{q}q - \pi\pi$ system, which allows us to extract the p-wave scattering phase at five values of pion relative momenta near the resonance region. The effective range formula describes the phase-shift dependence nicely, and we extract the resonance mass $m_\rho = 792(7)(8)$ MeV and the coupling $g_{\rho\pi\pi} = 5.13(20)$ at our $m_\pi \simeq 266$ MeV. The coupling $g_{\rho\pi\pi}$ is directly related to the width of the ρ meson, and our value is close to the value derived from the experimental width. The simulations are performed using dynamical gauge configurations with two mass-degenerate flavors of tree-level improved clover-Wilson fermions. Correlation functions are calculated using the recently proposed distillation method with Laplacian-Heaviside smearing of quarks, which enables flexible calculations, in many cases with unprecedented accuracy.

DOI: 10.1103/PhysRevD.84.054503 PACS numbers: 11.15.Ha, 12.38.Gc

I. MOTIVATION AND INTRODUCTION

Almost all hadrons listed in the Particle Data Group [1] tables are unstable, most of them decaying strongly. In quenched calculations, where vacuum quark loops are disregarded, all hadronic states appear as stable states. In full QCD, on the other hand, truly asymptotic exponential behavior is always dominated by the lowest stable end product. This is unsatisfactory.

In continuum physics experiments resonances are identified via the scattering cross section and subsequent phase-shift analyses. In the lattice discretization of QCD, instead, one studies the correlation functions of hadron interpolators for Euclidean time distances. The result is a combination of exponentially decaying terms, each corresponding to the energy level of a contributing eigenstate. Because of the finiteness of the lattice system, the energy levels are discrete. The spectral density is related to a discretization of the cross section. However, in realistic lattice simulations only very few such levels can be determined. The typical gaps are $\mathcal{O}(2\pi/L)$ for lattices of spatial extent L; for most simulations this corresponds to level spacing $\mathcal{O}(400)$ MeV.

However, as has been pointed out in a seminal paper by Lüscher [2,3], for a resonating system the discrete spectrum obtained in a finite volume can be related to the phase shift of the continuum scattering amplitude in the elastic region. The resulting volume dependence of the spectrum can then be used to explore the resonance properties [4]. Model simulations in two dimensions [5] as well as in four dimensions [6] demonstrated the feasibility of that approach. The original derivation in the decaying particles rest frame was then extended to moving frames [7–9], thus enhancing the practical applicability, allowing one to obtain the phase shift at more momentum points for a given lattice size. Because of several problems there have only been a few attempts to apply Lüscher's proposal to the decay $\rho \rightarrow \pi\pi$ [9–14], while the first lattice estimate of the $\rho \rightarrow \pi\pi$ amplitude [15] did not apply Lüscher's method. Note that widths for most of the other resonances have not been determined on the lattice at all.

There are two major complications. The first one concerns the hadronic lattice interpolators used. Let us assume that we work with the fully dynamic vacuum, i.e., including the dynamical quark vacuum loops in a full QCD simulation. Naively one would expect that, even if one correlates only quark-antiquark interpolators with the correct quantum numbers of the ρ, due to the vacuum loops, $\pi\pi$ intermediate states should also contribute and affect the energy levels accordingly. This is hardly observed; actually, already in model calculations [5] it proved necessary to include both the heavy boson and the two light bosons in the set of interpolators. Similar observations were made in other calculations involving baryon and meson correlation functions [16–19]. The obvious interpretation is that the overlap of the quark-antiquark interpolators with the meson-meson decay channel interpolators is too weak to have been observed.

For that reason one should extend the set of hadron interpolators to include both various versions of the quark-antiquark interpolator (like, e.g., different Dirac structure or

---

[*] christian.lang@uni-graz.at
[†] mohler@triumf.ca
[‡] sasa.prelovsek@ijs.si

different quark smearing functions) and meson-meson interpolators. The latter involve four propagating fermions, and the corresponding entries of the correlation function usually will involve backtracking loops. In addition to this technical complication, there is also the notorious issue of statistical weight for such contributions. The so-called distillation [or Laplacian-Heaviside (LapH) quark smearing] method introduced in [20] and employed in [19,21–24] helps us significantly to deal with that problem.

The second challenge concerns the energy levels. One works with several hadronic interpolators, all with the correct quantum numbers and total momentum in the given channel. The diagonalization of the correlation matrix gives the eigenstates and eigenenergies according to the so-called variational method [25–28]. The set of lattice interpolators should be large enough to be able to represent the leading eigenstates and thus the leading energy levels. The better the set is, the better the results will be and the more energy levels can be determined, depending of course also on the available statistics. In previous calculations aimed at ρ meson decay, at most two interpolators were used: one quark-antiquark and one pion-pion interpolator. We extend this to a larger interpolator basis.

For our calculation we use one lattice ensemble with $n_f = 2$ dynamical mass-degenerate light quarks and clover-improved Wilson fermionic action (generated in the context of the work [29,30] in order to study reweighting techniques). The ensemble consists of $16^3 \times 32$ lattices with spatial extent 1.98 fm and $m_\pi \simeq 266$ MeV. We consider cross correlations of several interpolators (16 for the ρ channel, six for the pion channel) and solve the generalized eigenvalue problem to reliably determine the two lowest energy levels. We study the ρ channel for three values of the total momentum and obtain the elastic phase shift in the resonance region.

Section II gives an overview of the methods: quarks sources, interpolators, variational analysis, phase-shift relations, and finite time effects. In Sec. III the set of configurations and details on the computations are summarized, and in Sec. IV we discuss the results: correlation functions, energy levels, phase shift, and resonance parameters.

Reference [31] suggests an alternative approach which has recently been investigated in [32]. Furthermore, another procedure has been suggested in [33].

II. TOOLS

A. Phase-shift formulas, brief review

On finite lattices there are, strictly speaking, no asymptotically free states, and the energy spectrum is always discrete. It was pointed out by Lüscher [3,4] that, assuming a localized interaction range, the energy level of a correlation matrix for channels with resonances in a finite volume can be related to the corresponding phase shift in infinite volume in the elastic region (i.e., where only one decay channel is open). The relation was derived for interpolators with spatial momentum zero. For a particle like the ρ meson, which can decay into two pions with back-to-back momenta, the available momenta are discrete on finite lattices and depend on the spatial extent.

In the noninteracting case the various two-pion energy levels will decrease with growing volume, and this leads to level crossing with the stable ρ state. If the interaction is switched on, the level crossing is avoided and the energy levels "change their identity." This was demonstrated in a two-dimensional resonance model in [5] as well as in four-dimensional ϕ^4-model simulations [6].

For the analysis of resonances in that method, one needs several ingredients. The set of interpolators should overlap with both the single particle content (i.e., for a meson, the quark-antiquark component) and the two particle content (i.e., the meson-meson decay channel). Furthermore, it should be possible to analyze more levels than just the ground state energy. Third, in the originally proposed method one needs several spatial volumes to obtain the phase shift at several values of relative momentum. This makes the approach costly.

The third aspect can be ameliorated, though, by also studying channels with nonvanishing total momentum,

$$\mathbf{P} = \frac{2\pi}{L}\mathbf{d} \quad \text{with} \quad \mathbf{d} \in \mathbb{Z}^3. \tag{1}$$

In our simulation we study the cases

$$\mathbf{d} = (0,0,0),\ (0,0,1),\ (1,1,0) \tag{2}$$

and permutations, which have previously been combined in the simulation [13]. Different values of $\mathbf{P}$ allow us to obtain the phase shifts at different values of pion relative momenta. The lowest $\pi\pi$ state in the ρ channel with $|\mathbf{P}| = 0$ is $\pi(2\pi/L)\pi(-2\pi/L)$ (due to $\ell = 1$) and is significantly above the ρ resonance in typical simulations. In the case of a ρ with $|\mathbf{P}| = 2\pi/L$, the $\pi(0)\pi(2\pi/L)$ is closer to the resonance region, for example. However, this case involves relativistic kinematics in the nonzero momentum frame, as pointed out in [7–9]. The relativistic distortion reduces the full cubic symmetry O_h to that of prismatic dihedral groups, i.e., to the symmetry of a cuboid (quadratic prism) D_{4h} for total momenta of type (0,0,1) and to the symmetry of a rhombic prism D_{2h} for momentum (1,1,0).

In the laboratory frame, the total three-momentum of two *noninteracting* bosons in a cubic lattice of volume L^3 and periodic boundary conditions is

$$\mathbf{P} = \mathbf{p}_1 + \mathbf{p}_2 = \frac{2\pi}{L}\mathbf{d} \tag{3}$$

and the energy is

$$E = E_1 + E_2 = \sqrt{m^2 + \mathbf{p}_1^2} + \sqrt{m^2 + \mathbf{p}_2^2} \quad \text{with} \quad \mathbf{p}_i = \frac{2\pi}{L}\mathbf{n}_i,\ \mathbf{n}_i \in \mathbb{Z}^3. \tag{4}$$

The velocity $\mathbf{v} = \mathbf{P}/E$ gives the relativistic boost factor $\gamma = 1/\sqrt{1 - \mathbf{v}^2}$. In the center-of-momentum frame (CMF) the total momentum vanishes and the boson momenta are

$$\mathbf{p}_1^* = -\mathbf{p}_2^* \equiv \mathbf{p}^*. \tag{5}$$

The energy in the CMF is

$$E_{\mathrm{CM}} = 2\sqrt{m^2 + \mathbf{p}^{*2}} = E/\gamma, \tag{6}$$

and the momentum is related to the laboratory frame through

$$\mathbf{p}^* = \tfrac{1}{2}\gamma_{op}^{-1}(\mathbf{p}_1 - \mathbf{p}_2), \tag{7}$$

where the boost factor acts in the direction of $\mathbf{v}$,

$$\gamma_{op}^{-1}\mathbf{p} \equiv \mathbf{p}_{\|}/\gamma + \mathbf{p}_{\perp}, \qquad \mathbf{p}_{\|} = \mathbf{v}(\mathbf{p}\cdot\mathbf{v})/|\mathbf{v}|^2,$$
$$\mathbf{p}_{\perp} = \mathbf{p} - \mathbf{p}_{\|}. \tag{8}$$

The relativistic four-momentum squared is invariant; thus the relation to the laboratory energy E is

$$E_{\mathrm{CM}}^2 = E^2 - \mathbf{P}^2 \rightarrow \mathbf{p}^{*2} = \tfrac{1}{4}E_{\mathrm{CM}}^2 - m^2. \tag{9}$$

Because of the coarseness of the lattice we replace, in our calculations, this continuum dispersion relation by the lattice dispersions relation as suggested in [7], i.e.,

$$\cosh E_{\mathrm{CM}}a = \cosh Ea - 2\sum_{k=1}^{3}\sin^2\left(\frac{P_k a}{2}\right), \tag{10}$$

$$\left(2\sin\frac{ap^*}{2}\right)^2 = 2\cosh\frac{E_{\mathrm{CM}}a}{2} - 2\cosh ma. \tag{11}$$

For the *interacting* case, the momenta $p_{1,2}$ of individual pions in the laboratory frame are no longer multiples of $2\pi/L$. Assuming a localized interaction region, one associates the outside region with that of two free bosons. The observed energy levels E_n are shifted and related to the scattering phase shift. Expressed through the CMF variable

$$\mathbf{p}^{*2} \equiv \left(q\frac{2\pi}{L}\right)^2, \tag{12}$$

one obtains relations of the form $\tan\delta(q) = f(q)$ for transcendental functions $f(q)$.

We concentrate on the decay $\rho \rightarrow \pi\pi$, where the two pions are in the p wave ($\ell = 1$). Details have been discussed in the original papers [3,4,7–9,13]. For completeness, we summarize here only the relevant final expressions, where phase shifts are expressed in terms of the generalized zeta function defined by

$$\mathcal{Z}_{\ell m}^{\mathbf{d}}(s; q^2) = \sum_{\mathbf{x}\in P_{\mathbf{d}}} \frac{\mathcal{Y}_{\ell m}^*(\mathbf{x})}{(\mathbf{x}^2 - q^2)^s},$$
$$P_{\mathbf{d}} = \left\{\mathbf{x} \in \mathbb{R}^3 \mid \mathbf{x} = \gamma_{op}^{-1}\left(\mathbf{m} + \frac{\mathbf{d}}{2}\right), \mathbf{m} \in \mathbb{Z}^3\right\},$$
$$\mathcal{Y}_{\ell m}(\mathbf{x}) = |\mathbf{x}|^{\ell} Y_{\ell m}(\mathbf{x}), \tag{13}$$

and $\mathcal{Y}_{\ell m}$ are the harmonic polynomials to the spherical harmonics functions $Y_{\ell m}$. The zeta function has to be analytically continued to $s = 1$. The simpler form for $\mathbf{d} = 0$ is given in [3]. A rapidly convergent expression for nonvanishing $\mathbf{d}$ is derived in [9]. We numerically compared the different representations of the zeta functions of [8,9] and found agreement.

The symmetry groups of the sum appearing in Z_{lm} (13) are O_h, D_{4h}, and D_{2h}, respectively, for $d = (0, 0, 0)$, (0, 0, 1), and (1, 1, 0). The $J^P = 1^-$ states appear in the specific representations of these symmetry groups, and the final expressions for the phase shifts are as follows:

Zero momentum $P = (0, 0, 0)$ (for irrep. T_1^- in O_h) [3]:

$$\tan\delta(q) = \frac{\pi^{3/2}q}{\mathcal{Z}_{00}(1; q^2)}. \tag{14}$$

Nonzero momentum $P = (0, 0, 1)\frac{2\pi}{L}$ (for irrep. A_2^- in D_{4h}) [7]:

$$\tan\delta(q) = \frac{\gamma\pi^{3/2}q^3}{q^2\mathcal{Z}_{00}^{\mathbf{d}}(1; q^2) + \sqrt{\frac{4}{5}}\mathcal{Z}_{20}^{\mathbf{d}}(1; q^2)}. \tag{15}$$

Nonzero momentum $P = (1, 1, 0)\frac{2\pi}{L}$ (for irrep. B_1^- in D_{2h}) [13]:

$$\tan\delta(q) = \frac{\gamma\pi^{3/2}q^3}{q^2\mathcal{Z}_{00}^{\mathbf{d}}(1; q^2) - \sqrt{\frac{1}{5}}\mathcal{Z}_{20}^{\mathbf{d}}(1; q^2) + \mathrm{i}\sqrt{\frac{3}{10}}(\mathcal{Z}_{22}^{\mathbf{d}}(1; q^2) - \mathcal{Z}_{2\bar{2}}^{\mathbf{d}}(1; q^2))}. \tag{16}$$

We independently derived this relation and we agree with this expression, originally presented in [9,13].

B. Variational analysis

To extract the lowest two energy levels with the quantum numbers $I^G(J^{\mathrm{PC}}) = 1^+(1^{--})$ of the ρ meson as well as the ground state energies with quantum numbers $I^G(J^{\mathrm{PC}}) = 1^-(0^{-+})$ of the pion, we construct a matrix $C(t)_{ij}$ of lattice interpolating fields containing both quark-antiquark and meson-meson (in our case, pion-pion) interpolators,

$$C(t)_{ij} = \sum_n \mathrm{e}^{-tE_n}\langle 0|O_i|n\rangle\langle n|O_j^{\dagger}|0\rangle. \tag{17}$$

For this matrix, the generalized eigenvalue problem

$$C(t)\vec{\psi}^{(n)} = \lambda^{(n)}(t)C(t_0)\vec{\psi}^{(n)} \tag{18}$$

is solved for each time slice. For the eigenvalues $\lambda^{(n)}(t)$ one obtains

$$\lambda^{(n)}(t) \propto \mathrm{e}^{-tE_n}(1 + \mathcal{O}(\mathrm{e}^{-t\Delta E_n})), \tag{19}$$

so that each eigenvalue is dominated by a single energy at large time separations. This method is called the variational method [25–28]. For a detailed discussion of the energy difference ΔE_n, which is, in general, given by the difference between the energy level in consideration and the closest neighboring level, please refer to [28].

We calculate the eigenvector components of the regular eigenvector problem

$$C(t_0)^{-(1/2)}C(t)C(t_0)^{-(1/2)}\vec{\psi}^{(n)\prime} = \lambda^{(n)}(t)\vec{\psi}^{(n)\prime}. \tag{20}$$

In addition to the eigenvalues, the eigenvectors provide useful information and can serve as a fingerprint for a given state. To track the eigenvalue corresponding to a given energy over the full range of time separations, the eigenvalues have to be sorted, either by their magnitude or by scalar products of their eigenvectors. In the presence of backwards running contributions caused by the finite time extent of the lattice, a combination of both methods works well: the eigenvalues are sorted by magnitude at low time separations and by scalar products at larger time separations. For our analysis we choose this method.

C. Interpolators

For the ρ channel we employ 15 quark-antiquark interpolators and one pion-pion interpolator with $J^{PC} = 1^{--}$ and $|I, I_3\rangle = |1, 0\rangle$ in the variational basis for each of the three choices for $\mathbf{P}$ as given in (2). All previous simulations aimed at determining the ρ meson width used at most one quark-antiquark and one pion-pion interpolator and extracted the two lowest energy levels from a 2×2 variational basis. This may not be reliable if the third energy level is nearby and does not allow testing whether the resulting two levels are robust against the choice of interpolators. A larger basis enables us to exploit the dependence of the extracted energies on the choice of the interpolators. It also indicates whether the lowest two states can be reliably extracted using our quark-antiquark interpolators alone, or whether the pion-pion interpolators are required in the variational basis.

The 15 different quark-antiquark interpolators $\mathcal{O}^s_{\text{type}}$ (type $= 1, \ldots, 5$, $s = n, m, w$) differ in type (Dirac and color structure) and width of the smeared quarks q_s. We use three different smearing widths, $s = n, m, w$ (narrow, middle, wide), for individual quarks, and all quarks in a given interpolator have the same width s in this simulation. (Choosing different quark widths within an interpolator is a straightforward generalization, and one just needs to pay attention that the resulting C parity is correct.) The details on the smearing are given in Sec. II E. The interpolator $\mathcal{O}_6$ is the $\pi\pi$ interpolator whose structure is explained at the end of this subsection. Our 16 ρ interpolators are

$$\begin{aligned}
\mathcal{O}^s_1(t) &= \sum_{\mathbf{x},i}\frac{1}{\sqrt{2}}\bar{u}_s(x)A_i\gamma_i\mathrm{e}^{\mathrm{i}\mathbf{Px}}u_s(x) - \{u_s \leftrightarrow d_s\}; \qquad (s = n, m, w),\\
\mathcal{O}^s_2(t) &= \sum_{\mathbf{x},i}\frac{1}{\sqrt{2}}\bar{u}_s(x)\gamma_t A_i\gamma_i\mathrm{e}^{\mathrm{i}\mathbf{Px}}u_s(x) - \{u_s \leftrightarrow d_s\}; \qquad (s = n, m, w),\\
\mathcal{O}^s_3(t) &= \sum_{\mathbf{x},i,j}\frac{1}{\sqrt{2}}\bar{u}_s(x)\overleftarrow{\nabla}_j A_i\gamma_i\mathrm{e}^{\mathrm{i}\mathbf{Px}}\overrightarrow{\nabla}_j u_s(x) - \{u_s \leftrightarrow d_s\}; \qquad (s = n, m, w),\\
\mathcal{O}^s_4(t) &= \sum_{\mathbf{x},i}\frac{1}{\sqrt{2}}\bar{u}_s(x)A_i\frac{1}{2}[\mathrm{e}^{\mathrm{i}\mathbf{Px}}\overrightarrow{\nabla}_i - \overleftarrow{\nabla}_i\mathrm{e}^{\mathrm{i}\mathbf{Px}}]u_s(x) - \{u_s \leftrightarrow d_s\}; \qquad (s = n, m, w),\\
\mathcal{O}^s_5(t) &= \sum_{\mathbf{x},i,j,k}\frac{1}{\sqrt{2}}\epsilon_{ijl}\bar{u}_s(x)A_i\gamma_j\gamma_5\frac{1}{2}[\mathrm{e}^{\mathrm{i}\mathbf{Px}}\overrightarrow{\nabla}_l - \overleftarrow{\nabla}_l\mathrm{e}^{\mathrm{i}\mathbf{Px}}]u_s(x) - \{u_s \leftrightarrow d_s\}; \qquad (s = n, m, w),\\
\mathcal{O}^{s=n}_6(t) &= \frac{1}{\sqrt{2}}[\pi^+(\mathbf{p_1})\pi^-(\mathbf{p_2}) - \pi^-(\mathbf{p_1})\pi^+(\mathbf{p_2})], \qquad \pi^\pm(\mathbf{p_i}) = \sum_{\mathbf{x}}\bar{q}_n(x)\gamma_5\tau^\pm\mathrm{e}^{\mathrm{i}\mathbf{p_i}x}q_n(x).
\end{aligned} \tag{21}$$

In the pion interpolator $\tau^\pm$ denote the corresponding combination of Pauli matrices and the $\pi\pi$ interpolator $\mathcal{O}_6$ is always composed from narrow quarks. The covariant derivative (often denoted by $\vec{D}_i$)

$$\vec{\nabla}_i(\mathbf{x}, \mathbf{y}) = U_i(\mathbf{x}, 0)\delta_{\mathbf{x}+\mathbf{i},\mathbf{y}} - U_i^\dagger(\mathbf{x} - \mathbf{i}, 0)\delta_{\mathbf{x}-\mathbf{i},\mathbf{y}} \tag{22}$$

is used in some of the quark-antiquark interpolators (used already in a number of lattice simulations, e.g. [16,34]) and will also be employed to prepare smeared quarks q_s below. It acts on the spatial and color indices and leaves time and Dirac indices intact. The linear combinations in $\mathcal{O}_{4,5}$ are required for good C parity. The polarization vector $\mathbf{A}$ of the quark-antiquark vector current depends on the total momentum $\mathbf{P} = \frac{2\pi}{L}\mathbf{d}$ as

$$\begin{aligned} &\mathbf{d} = (0,0,0)\ \mathbf{A} = (0,0,1), \quad \mathbf{p_1} = -\frac{2\pi}{L}\mathbf{A}, \quad \mathbf{p_2} = \frac{2\pi}{L}\mathbf{A}. \\ &\mathbf{d} = (0,0,1)\ \mathbf{A} = \mathbf{d}, \quad \mathbf{p_1} = 0, \quad \mathbf{p_2} = \mathbf{P}. \\ &\mathbf{d} = (1,1,0)\ \mathbf{A} = \mathbf{d}, \quad \mathbf{p_1} = 0, \quad \mathbf{p_2} = \mathbf{P}. \end{aligned} \tag{23}$$

Our choices for $\pi\pi$ interpolators $\mathcal{O}_6$ (21) with momentum projections for individual pions (23) are the same as in [13]:

(i) For $\mathbf{d} = (0,0,0)$ with the symmetry group O_h, our interpolator transforms according to the three-dimensional representation T_1^- (so just like $\mathbf{e_z}$) under elements of O_h.

(ii) For $\mathbf{d} = (0,0,1)$ with the symmetry group D_{4h}, the interpolator transforms according to one-dimensional A_2^- (like $\mathbf{e_z}$) under elements of D_{4h}.

(iii) For $\mathbf{d} = (1,1,0)$ with the symmetry group D_{2h}, our interpolator transforms according to one-dimensional B_1^- (like $\mathbf{e_x} + \mathbf{e_y}$) under elements of D_{2h}. Note that the interpolator $\mathcal{O}_6$ with $\mathbf{p_1} = (1,0,0)$ and $\mathbf{p_2} = (0,1,0)$ has the same total momentum, but it has positive parity and it will not appear as an eigenstate for interpolators with B_1^- transformation properties.

For the isovector pion $J^{PC} = 0^{-+}$ correlation matrix we use, altogether, six interpolators, employing three smearing widths for each of the two Dirac structures,

$$\begin{aligned} &\mathcal{O}^{\pi}_{\text{type},s}(t) = \sum_{\mathbf{x}} \bar{u}_s(x)\Gamma_{\text{type}} e^{i\mathbf{Px}} d_s(x), \\ &\Gamma_1 = \gamma_5, \qquad \Gamma_2 = \gamma_5\gamma_t, \qquad s = n, m, w. \end{aligned} \tag{24}$$

D. Correlators and contractions

In the ρ channel we compute 16×16 correlation matrices for

$$C_{jk}(t_f, t_i) = \langle 0|\mathcal{O}_j(t_f)\mathcal{O}_k^\dagger(t_i)|0\rangle, \qquad j,k = 1,16, \tag{25}$$

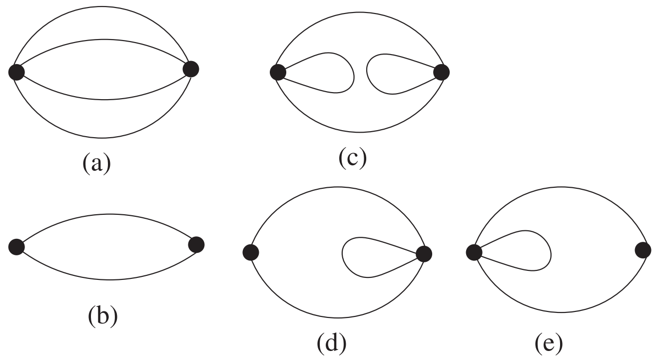

FIG. 1. Contractions for our correlators with $\bar{q}q$ and $\pi\pi$ interpolators.

where the indices j and k stand for the combination (type, s) in $\mathcal{O}_{\text{type},s}$ (21). These correlators involve (cf. Fig. 1) connected contractions (a,b), singly disconnected contractions (c), and contractions (d,e). Because of the momentum projections at the sink time slices t_f, the contractions (c) and (d), in particular, require the propagators M^{-1} from any spatial point at the sink time slice $t_f = 1, \ldots, N_T$.

E. Laplacian-Heaviside smearing for quarks and the distillation method

Since calculating all elements of M^{-1} for the fermion Dirac operator matrix M is prohibitively time consuming, we apply the distillation method proposed in [20]. This method is based on a special kind of smearing for quarks that allows treatment of all necessary contractions. All quarks are smeared according to a prescription similar to the conventional one, $q_s^{\text{Gauss}}(\mathbf{x}, t) = e^{\sigma_s \nabla^2} q(\mathbf{x}, t)$, where ∇^2 denotes the 3D lattice Laplacian acting in a time slice. The major simplification is due to the spectral decomposition[1]

$$f(A) = \sum_{k=1}^{N} f(\lambda^{(k)}) v^{(k)} v^{(k)\dagger} \tag{26}$$

for matrix $A = \nabla^2$, giving $e^{\sigma_s \nabla^2} = \sum_1^N e^{\sigma_s \lambda^{(k)}} v^{(k)} v^{(k)\dagger}$. Here $\lambda^{(k)}$ and $v^{(k)}$ are eigenvalues and eigenvectors of ∇^2 (22) which is a $N_L^3 N_c \times N_L^3 N_c$ matrix on a given gauge configuration

$$\nabla^2_{\mathbf{x}c,\mathbf{x}'c'}(t) v^{(k)}_{\mathbf{x}'c'}(t) = \lambda^{(k)}(t) v^{(k)}_{\mathbf{x}c}(t) \tag{27}$$

and all the resulting eigenvalues are negative. The choice of smearing is arbitrary, and instead of this Gaussian smearing, we use the truncated spectral representation of the unit operator (also called the LapH smearing), as proposed in [20] and employed also in [19,21–24],

$$\begin{aligned} q_s &\equiv \Theta(\sigma_s^2 + \nabla^2) q = \sum_{k=1}^{N_c N_L^3} \Theta(\sigma_s^2 + \lambda^{(k)}) v^{(k)} v^{(k)\dagger} q, \\ q_s^{\alpha c}(\mathbf{x}, t) &= \sum_{k=1}^{N_v} v^{(k)}_{\mathbf{x}c}(t) v^{(k)\dagger}_{\mathbf{x}'c'}(t) q^{\alpha c'}(\mathbf{x}', t) \\ &\equiv \square^{N_v}_{\mathbf{x}c,\mathbf{x}'c'} q^{\alpha c'}(\mathbf{x}', t), \\ &\alpha, \alpha' = 1, \ldots, N_d = 4, \quad c, c' = 1, \ldots, N_c = 3. \end{aligned} \tag{28}$$

The Heaviside smearing denoted by $\square^{N_v}$ is particularly suitable since it cuts away the terms for $k > N_v$, where the number of eigenvectors N_v kept in the sum depends on the chosen width $\sigma_{s=n,m,w}$. This choice of smearing reduces

---

[1] A is an $N \times N$ matrix with eigenvalues $\lambda^{(k)}$ and eigenvectors $v^{(k)}$, $Av^{(k)} = \lambda^{(k)} v^{(k)}$ $(k = 1, \ldots, N)$.

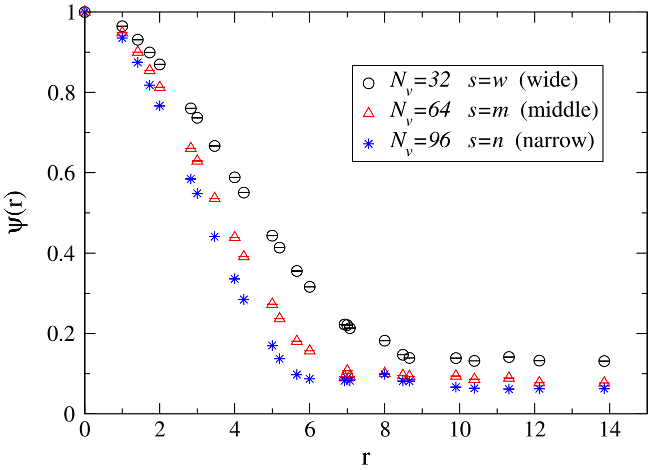

FIG. 2 (color online). The spatial distribution $\Psi(r)$ (30) of the distillation operator $\Box^{N_v}$ (28) constructed from the eigenvectors corresponding to the N_v lowest eigenvalues of the Laplace operator. The values are computed on each time slice of 49 configurations at distances along the main axes and diagonals and plotted only until their respective symmetry points. Circles (black), triangles (red), and stars (green) denote wide, middle, and narrow sources ($N_v = 32, 64, 96$), respectively.

the number of needed inversions (per time slice, Dirac index, and configuration) from the prohibitively large number $N_L^3 N_c$ (needed for the conventional all-to-all approach) to a manageable number $N_v \simeq O(100)$.

Different truncations correspond to different effective smearing widths. We choose three smearing widths for quarks,

$$\begin{aligned} N_v &= 96 \quad \text{for } s = n \text{ (narrow)}, \\ N_v &= 64 \quad \text{for } s = m \text{ (middle)}, \qquad (29) \\ N_v &= 32 \quad \text{for } s = w \text{ (wide)}, \end{aligned}$$

which lead to the spatial distributions [20] of

$$\Psi(r) = \sum_{\mathbf{x},t} \sqrt{\mathrm{Tr}_c[\Box_{\mathbf{x},\mathbf{x}+\mathbf{r}}(t)\Box_{\mathbf{x},\mathbf{x}+\mathbf{r}}(t)]} \qquad (30)$$

shown in Fig. 2.

We build each interpolator (21) from quarks of the same width for all three widths. This enlarges the variational basis and increases the possibility for optimal eigensets.

F. Evaluation of the correlators

The interpolators $\mathcal{O}_{1-5}$ given in (21) are linear combinations of quark-antiquark currents, which can be generally written as

$$\bar{Q}^{\alpha'c'}_s(\mathbf{x}',t)\Gamma_{\alpha'\alpha}\mathcal{F}^{c'c}_{\mathbf{x}'\mathbf{x}}(t,\mathbf{p})q^{\alpha c}_s(\mathbf{x},t), \qquad q, Q = u, d, \qquad (31)$$

where the shape function $\mathcal{F}(t, \mathbf{p})$ incorporates the momentum projection to $\mathbf{p}$ and the effect of covariant derivatives. Shape functions $\mathcal{F}$ for our interpolators (21) are given in (A3) of the Appendix. The pion-pion interpolator $\mathcal{O}_6$ is a linear combination of products of two currents (31).

After inserting the expression for smeared quarks q_s of (28) into interpolators (21), all the contractions for $C(t_f, t_i)$ can be expressed in terms of three quantities Γ, ϕ, and τ, analogous to the original proposal [20] which considered only one smearing width. Correlators are expressed in terms of the following:

(i) Dirac matrices Γ of size $N_d \times N_d$.

(ii) The interpolator shape matrices $\phi(t, \mathcal{F})$ are square matrices of size $N_v \times N_v$ for an interpolator with a given smearing width N_v,

$$\phi^{k'k}(t, \mathcal{F}) = \sum_{\mathbf{x}',\mathbf{x},c',c} v^{(k')\dagger}_{\mathbf{x}'c'}(t)\mathcal{F}^{c'c}_{\mathbf{x}'\mathbf{x}}(t, \mathbf{p})v^{(k)}_{\mathbf{x}c}(t). \qquad (32)$$

Our ϕ is related to Φ in [20] as $\Phi^{k'k}_{\alpha'\alpha} = \phi^{k'k}\Gamma_{\alpha'\alpha}$.

(iii) The so-called perambulator matrices $\tau^{k'k}(t', t)$ [20] denote the propagators from source of shape $v^k(t)$ to the sink of shape $v^{k'}(t')$,

$$\tau^{k'k}_{\alpha'\alpha}(t', t) \equiv \sum_{\mathbf{x}',\mathbf{x},c',c} v^{(k')\dagger}_{\mathbf{x}'c'}(t')(M^{-1})^{c'c}_{\alpha'\alpha}(\mathbf{x}', t'; \mathbf{x}, t)v^{(k)}_{\mathbf{x}c}(t). \qquad (33)$$

Our correlators depend on the perambulators $\tau(t_f, t_i)$, $\tau(t_i, t_f)$, $\tau(t_i, t_i)$, $\tau(t_f, t_f)$. These are, in general, rectangular matrices of sizes $N_d N_v^f \times N_d N_v^i$, $N_d N_v^i \times N_d N_v^f$, $N_d N_v^i \times N_d N_v^i$, and $N_d N_v^f \times N_d N_v^f$, respectively, where $N_v^{i,f} = 32, 64, 96$ denote the smearing widths of the source or sink.

The analytic expressions for the needed contractions (Fig. 1) in terms of Γ, τ, and ϕ are given in the Appendix.

We precalculated and stored the perambulators $\tau(t_f, t_i)$ from all source time slices $t_i = 1, \ldots, N_T = 32$ to all sink time slices $t_f = 1, \ldots, N_T = 32$. This allows us to compute all needed contractions for $C(t_f, t_i)$ straightforwardly. We sum[2] $C(t_f, t_i)$ over all initial time slices t_i to decrease the relative errors on the resulting correlators $C(t = t_f - t_i)$.

We also sum over the results for the three ρ polarizations $\mathbf{A} = (0, 0, 1)$, $(0, 1, 0)$, $(1, 0, 0)$ for $\mathbf{d} = (0, 0, 0)$, or sum over the directions $\mathbf{d} = (0, 0, 1)$, $(0, 1, 0)$, $(1, 0, 0)$ for $|\mathbf{d}| = 1$, and over the directions $\mathbf{d} = (1, 1, 0)$, $(0, 1, 1)$, $(1, 0, 1)$ for $|\mathbf{d}| = \sqrt{2}$. So, our final correlation matrices are

$$C_{jk}(t = t_f - t_i) = \sum_{t_i = 1,\ldots,N_T} \sum_{\mathbf{A} \text{ or } \mathbf{d}} C_{jk}(t_f, t_i). \qquad (34)$$

These correlation functions finally enter the variational analysis (18) to provide the energy levels.

---

[2] The sum plays the role of an average here.

G. Finite N_T effects and the "$P + A$" trick

Our dynamical quarks have antiperiodic boundary conditions in time. Using the valence quarks with the same antiperiodic boundary condition in time, we find that the finite time extent $N_T = 32$ ($T = 3.96$ fm) severely affects the eigenvalues $\lambda(t)$ near $t \simeq N_T/2 = 16$. There are two major sources for this:

(i) The $\pi(\mathbf{p_1})\pi(\mathbf{p_2})$ state receives contributions from both pions traveling forward or both traveling backward in time. But it also receives the contribution from $\pi(\mathbf{p_1})$ traveling forward and $\pi(\mathbf{p_2})$ traveling backward in time, and vice versa [35,36]. As a result, the cosh-type effective mass for some of the eigenvalues is not flat at $t > 11$.

(ii) In the pion channel, the ground state starts to dominate the second largest eigenvalue (and vice versa) at some moderate t [34,37].

We use a previously applied trick, which effectively extends the time direction to $2N_T = 64$ by combining the periodic propagator M_P^{-1} and antiperiodic propagator M_A^{-1} (see, for example, [36,38]). All results in this paper have been obtained using the so-called "$P + A$" propagators

$$M^{-1}_{\mathrm{P+A}}(t_f, t_i) = \begin{cases} \frac{1}{2}[M_P^{-1}(t_f, t_i) + M_A^{-1}(t_f, t_i)] & t_f \geq t_i \\ \frac{1}{2}[M_P^{-1}(t_f, t_i) - M_A^{-1}(t_f, t_i)] & t_f < t_i. \end{cases} \tag{35}$$

All our eigenvalues obtained from M^{-1}_{P+A} agree with those obtained from M_A^{-1} at $t \leq 11$. In the case of M_A^{-1}, the finite T effects seriously affect some of the eigenvalues for $t > 11$. In the case of M^{-1}_{P+A}, the finite T effects never show up in any of the ρ eigenvalues for $t \leq 16$, which allows us stable fit ranges at least until $t = 16$.

The $P + A$ trick is not a valid field theoretic prescription, since the valence quarks do not have the same periodicity as the dynamical quarks (which remain antiperiodic in time). In practice, the pion correlators with zero momentum, for example, are perfectly consistent with periodicity $2N_T$; i.e. they are proportional to $\mathrm{e}^{-m_\pi t} + \mathrm{e}^{-m_\pi(2T-t)}$ and keep falling until $t = 32$. We note that some of the nonzero momentum ρ correlators do not keep falling until $t = 32$, as would have been expected in the case of the proper field theoretic prescription. However, none of the ρ correlators show finite T effects for $t < 16$, which is the time window used for our analysis.

III. COMPUTATIONS

For the calculations presented here we use configurations generated for the study of reweighting techniques in the p regime of chiral perturbation theory (ChPT). A description of the normalized hypercubic smearing (nHYP smearing) used in the dynamic fermion action can be found in [39]. Results from simulations with this action have previously been published in [29,30], and the authors kindly provided the gauge configurations used in this study. The action used to generate the gauge configurations containing $n_f = 2$ flavors of mass-degenerate light quarks is a tree-level improved Wilson-Clover action with gauge links smeared using one level of nHYP smearing. Table I lists the parameters used for the simulation along with the number of (approximately independent) gauge configurations used and the pion mass resulting from the determination of the lattice scale detailed in the next subsection.

TABLE I. Configurations used for the current study. N_L and N_T denote the number of lattice points in spatial and time directions. For the determination of the lattice spacing a, please refer to Sec. III. The first error on m_π is statistical while the second error is from the determination of the lattice scale.

$N_L^3 \times N_T$	κ	β	a (fm)	L (fm)	Number of configs.	m_π (MeV)
$16^3 \times 32$	0.1283	7.1	0.1239(13)	1.98	280	266(3)(3)

The gauge field obeys a periodic boundary condition in time, while dynamical quarks are antiperiodic in time. As discussed in Sec. II G, we compute and combine valence quark propagators with both antiperiodic and periodic boundary conditions.

On each gauge configuration we calculate the lowest 96 eigenvectors of the lattice Laplacian on every time slice using a standard three-point stencil. Throughout, the gauge links are four-dimensional nHYP smeared with the same parameters used for generating the gauge configurations: $(\alpha_1, \alpha_2, \alpha_3) = (0.75, 0.6, 0.3)$. For the calculation of the eigenmodes and the interpolating fields containing covariant derivatives, we also experimented with additional three-dimensional link smearing (using regular HYP smearing) and found only mild effects on the quality of simple meson two-point correlators. We therefore opted to use no additional link smearing. For the calculation of the eigenmodes we use the PRIMME package [40]. In particular, the routine JDQMR_ETOL results in a fast determination for a small to moderate number [$\mathcal{O}(10)$ to $\mathcal{O}(100)$] of eigenmodes. For a larger number of eigenmodes the Arnoldi/Lanczos method (and variants) eventually outperform this method. For the methods implemented in PRIMME we also tried a preconditioner using Chebychev polynomials, very similar to the method described in [18]. While this greatly improved the performance of some methods, our preferred method was largely unaffected and still outperformed all other PRIMME methods for a moderate number of eigenmodes.

For the determination of the quark propagators we use the DFL_SAP_GCR algorithm provided in Lüscher's DDHMC package [41,42]. Because of the large number of sources necessary for the distillation approach, an inverter employing low-mode deflation techniques is especially well suited. For the case presented here we observed a speedup factor of approximately 5 compared to a BICGSTAB

TABLE II. The ground state pion energy extracted for three momenta: E is extracted from the variational analysis using the chosen interpolator sets, while $E^{\text{d.r.}}$ are obtained using the ground state pion mass and the continuum and lattice dispersion relations (10).

$\mathbf{P}\frac{L}{2\pi}$	t_0	Interpolator	Fit range	χ^2/d.o.f.	Ea (simul.)	$E^{\text{d.r.}}_{\text{cont}}a$	$E^{\text{d.r.}}_{\text{lat}}a$
(0, 0, 0)	3	$\mathcal{O}^w_{1,2}\mathcal{O}^m_{1,2}\mathcal{O}^n_{1,2}$	8–14	1.57/5	$m_\pi a = 0.1673(16)$	$\cdots$	$\cdots$
(0, 0, 1)	3	$\mathcal{O}^w_2\mathcal{O}^n_2$	12–17	0.98/4	0.4374(64)	0.4268(65)	0.4215(65)
(1, 1, 0)	4	$\mathcal{O}^w_2\mathcal{O}^n_1$	8–13	1.31/4	0.5823(46)	0.5800(48)	0.5690(47)

algorithm without low-mode deflation, while the computing time needed to generate the deflation subspace was negligible compared to the actual calculation of quark propagators. Notice that this difference gets more pronounced for the lighter quark masses needed for future studies at or close to the physical point.

Statistical errors are determined with a single elimination jackknife procedure throughout. When extracting energy levels we properly account for correlation in Euclidean time t by estimating the full covariance matrix in the given fit interval. For the covariance matrix we use a jackknife estimate which is calculated on the ensemble average only.[3]

We determine the lattice spacing using the Sommer parameter [44]. We extract the static potential from planar Wilson loops $W(r, t)$ obtained on gauge configurations smeared with hypercubic blocking [45] with standard parameter values $(\alpha_1, \alpha_2, \alpha_3) = (0.75, 0.6, 0.3)$. The potential is computed for each value of r from linear fits to $\log W(r, t)$ in the range $t = 4\ldots7$ and then fitted to the lattice corrected form

$$V(r) = A + \frac{B}{r} + \sigma r + C\left(\left[\frac{1}{\mathbf{r}}\right] - \frac{1}{r}\right) \tag{36}$$

in the range $1 \leq r \leq 7$ or to the continuum form (i.e., $C = 0$) in the range $2 \leq r \leq 7$. Both values agree within less than 1 standard deviation. The lattice corrections involve the lattice Coulomb potential $[1/\mathbf{r}]$ corrected for the hypercubic blocking [46,47]. To convert our numbers to physical units (cf. Table I) we assume for the Sommer parameter the value $r_0 = 0.48$ fm and obtain $a = 0.1239(13)$ fm.

IV. RESULTS

A. Pion results

The pion energies are extracted from the variational analysis of the six interpolators given in (24). The extracted pion mass and pion energies for the two lowest nonzero momenta are given in Table II, along with the analytic predictions from the continuum and lattice dispersion relations.

B. Rho meson results

1. Energy levels

An example of the resulting correlators for interpolators $\pi\pi = \mathcal{O}_6$ and $\bar{q}q = \mathcal{O}_1$, and their cross correlators, are given in Fig. 3.

Given our 16×16 correlation matrices (21), we extracted the two lowest energy levels for a number of different submatrices (i.e., interpolator sets) of dimension 6×6 or less. Resulting levels for eight different choices of interpolator sets are shown in Fig. 4. The extracted ground state energy is robust with regard to the choice of the interpolator set, while the first excited energy is robust only if the interpolator set includes the $\pi\pi$ interpolator and if the correlation matrix is larger than 2×2. The first five choices include $\pi\pi$ in the interpolator basis, while the last three do not. The first excited energy for $d = (0, 0, 0)$ and $d = (0, 0, 1)$ has much larger errors and is often substantially higher if $\pi\pi$ is not in the set. On the other hand, it seems that the first excited energy in the case $d = (1, 1, 0)$ can be extracted also without a $\pi\pi$ interpolator in the set. The choice set $= 5$ shows the result from the two-dimensional basis $\pi\pi = \mathcal{O}_6$ and $\bar{q}q = \mathcal{O}_1$, which was used by some previous simulations [10,12–14]. Figure 4 indicates that such a choice gives a reasonable estimate for the first excited energy in the cases $d = (0, 0, 0)$ and

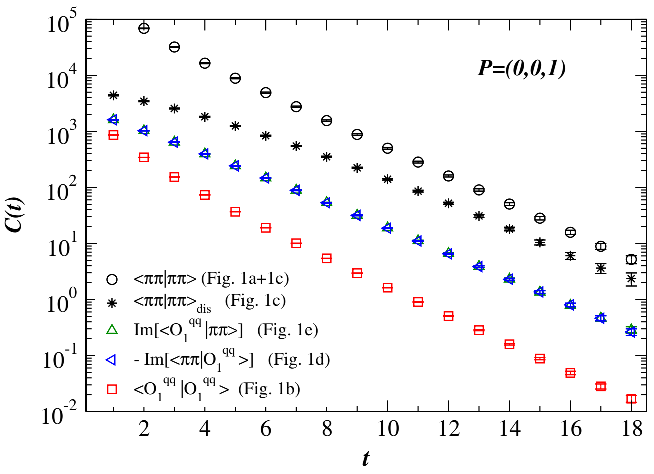

FIG. 3 (color online). An example of correlators for interpolators $\mathcal{O}_6 = \pi\pi$ and $\mathcal{O}^n_1$ and their cross correlators.

---

[3] This procedure has been referred to as *jackknife reuse* in [43].

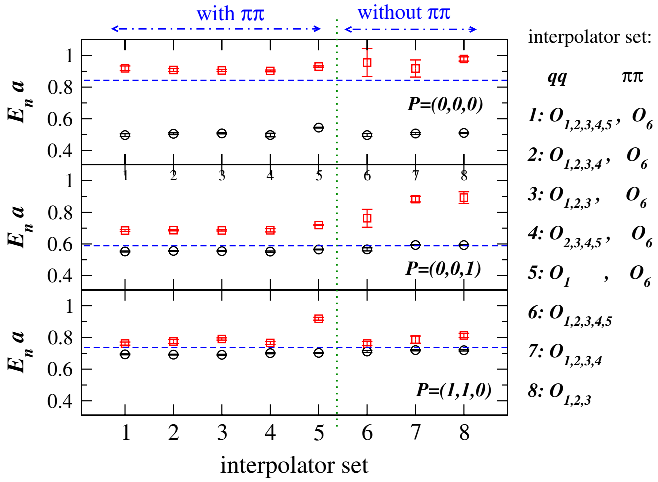

FIG. 4 (color online). The lowest two energy levels (circles denoting the ground state, squares the first excited state) extracted using different submatrices (interpolators sets) of the full 16×16 correlation matrix (21), all for $t_0 = 4$. The horizontal dashed lines indicate the energy values for two noninteracting pions. The interpolators $\mathcal{O}_{1\text{–}5}$ have $\bar{q}q$ valence structure, while $\mathcal{O}_6 = \pi\pi$. All interpolators in this plot are composed of narrow quarks $q_s = q_n$, with the exception of interpolator set 3 which is $\mathcal{O}_1^w \mathcal{O}_2^m \mathcal{O}_3^n \mathcal{O}_6^n$. In order to make different interpolator choices comparable, we use the same fit range $t = 7\text{–}10$ in the one-exponential correlated fit for the purpose of this figure [with the exception of $E_2(d = 0)$ obtained for $t = 5\text{–}7$].

$d = (0, 0, 1)$, while it gives a much higher energy for the first excited state with $d = (1, 1, 0)$. Our study shows that a basis larger than 2×2 is needed to extract the first excited level in this case.

Given that our lowest two energy levels are robust with respect to the choice of interpolator set, provided the set is large enough and contains the $\pi\pi$ interpolator, we present the final interpolator set choices in Table III. The corresponding effective masses for our preferred interpolator choices are shown in Fig. 5. The final values for the six energy levels in Table III are extracted using correlated two-exponential fits with t_0 as indicated in the table and starting at a rather small time separation t. We verified that the extracted levels agree with results obtained from one-exponential fits starting at larger t and using $t_0 = [2, 5]$.

2. Phase shifts and resonance parameters

Each of the energy levels of Table III gives the value of the scattering phase shift $\delta(s)$ at a different pion CMF momentum p^*. We employed the lattice dispersion relation (10) to get $p^* = \frac{2\pi}{L} q$ and used the phase-shift formulas in Sec. II A to get $\delta(q^2)$. Our results, including jackknife error estimates, are also given in Table III.

The resulting phase shift is related to the relativistic Breit-Wigner form for the elastic p-wave amplitude in the resonance region [1]

$$a_1 = \frac{-\sqrt{s}\Gamma(s)}{s - m_\rho^2 + \mathrm{i}\sqrt{s}\Gamma(s)} = \mathrm{e}^{\mathrm{i}\delta(s)} \sin\delta(s), \tag{37}$$

where $s = E_{\mathrm{CM}}^2$ is the Mandelstam variable and m_ρ^2 is the resonance position. Relation (37) can be conveniently written for later use as

$$\sqrt{s}\Gamma(s) \cot\delta(s) = m_\rho^2 - s, \tag{38}$$

and the decay width $\Gamma(s)$ is expressed in terms of the coupling constant $g_{\rho\pi\pi}$, taking into account the $\pi\pi$ phase space [48,49]

$$\Gamma(s) = \frac{p^{*3}}{s} \frac{g_{\rho\pi\pi}^2}{6\pi}, \tag{39}$$

where the ρ width $\Gamma_\rho = \Gamma(m_\rho^2)$ is evaluated at the resonance position.

The final relation, the so-called effective range formula, combines (38) and (39) and is valid in the elastic region $s < (4m_\pi)^2$,

$$\frac{p^{*3}}{\sqrt{s}} \cot\delta(s) = \frac{6\pi}{g_{\rho\pi\pi}^2}(m_\rho^2 - s). \tag{40}$$

It allows a linear fit for the two unknown parameters $6\pi/g_{\rho\pi\pi}^2$ and $6\pi m_\rho^2/g_{\rho\pi\pi}^2$. Values of s, p^*, and δ for the energy levels E_n are given in Table III, and appropriate combinations (40) are plotted in Fig. 6. In the fit and in the figures we do not include the first excited state with $P = 0$, since this lies above the 4π inelastic threshold.

Figure 6 shows the result of the linear fit to the data, giving our final result for $g_{\rho\pi\pi}$ and the mass of the ρ resonance [at our $m_\pi = 266(3)(3)$ MeV],

TABLE III. Final results for the lowest two ρ energy levels, all obtained using 2-exp correlated fits with given χ^2/d.o.f.. The choice of interpolator basis (21) is indicated. The pion momenta ap^* in the CMF and scattering phases δ are obtained using the lattice dispersion relation (10) and $m_\pi a$ in Table II. The state $E_2(P = 0)$ is above the 4π threshold and is denoted by a star.

$\mathbf{P}\frac{L}{2\pi}$	Level n	t_0	Interpolator	Fit range	$E_n a$	χ^2/d.o.f.	ap^*	sa^2	δ
(0, 0, 0)	1	2	$\mathcal{O}^n_{1,2,3,4,6}$	3–18	0.5107(40)	6.10/12	0.1940(29)	0.2608(41)	130.56(1.37)
(0, 0, 0)	2	2	$\mathcal{O}^n_{1,2,3,4,6}$	3–12	0.9002(101)	0.85/6	0.4251(58)	0.8103(182)	146.03 (6.58) [*]
(0, 0, 1)	1	2	$\mathcal{O}^n_{1,2,3,4,6}$	4–16	0.5517(26)	4.06/9	0.1076(36)	0.1579(29)	3.06 (0.06)
(0, 0, 1)	2	2	$\mathcal{O}^n_{1,2,3,4,6}$	4–15	0.6845(49)	3.10/8	0.2329 (40)	0.3260(69)	156.41(1.56)
(1, 1, 0)	1	3	$\mathcal{O}^n_{1,2,3,6}$	4–12	0.6933(33)	4.33/5	0.1426(42)	0.1926(49)	6.87(0.38)
(1, 1, 0)	2	3	$\mathcal{O}^n_{1,2,3,6}$	4–12	0.7868(116)	2.34/5	0.2392(101)	0.3375(191)	164.25(3.53)

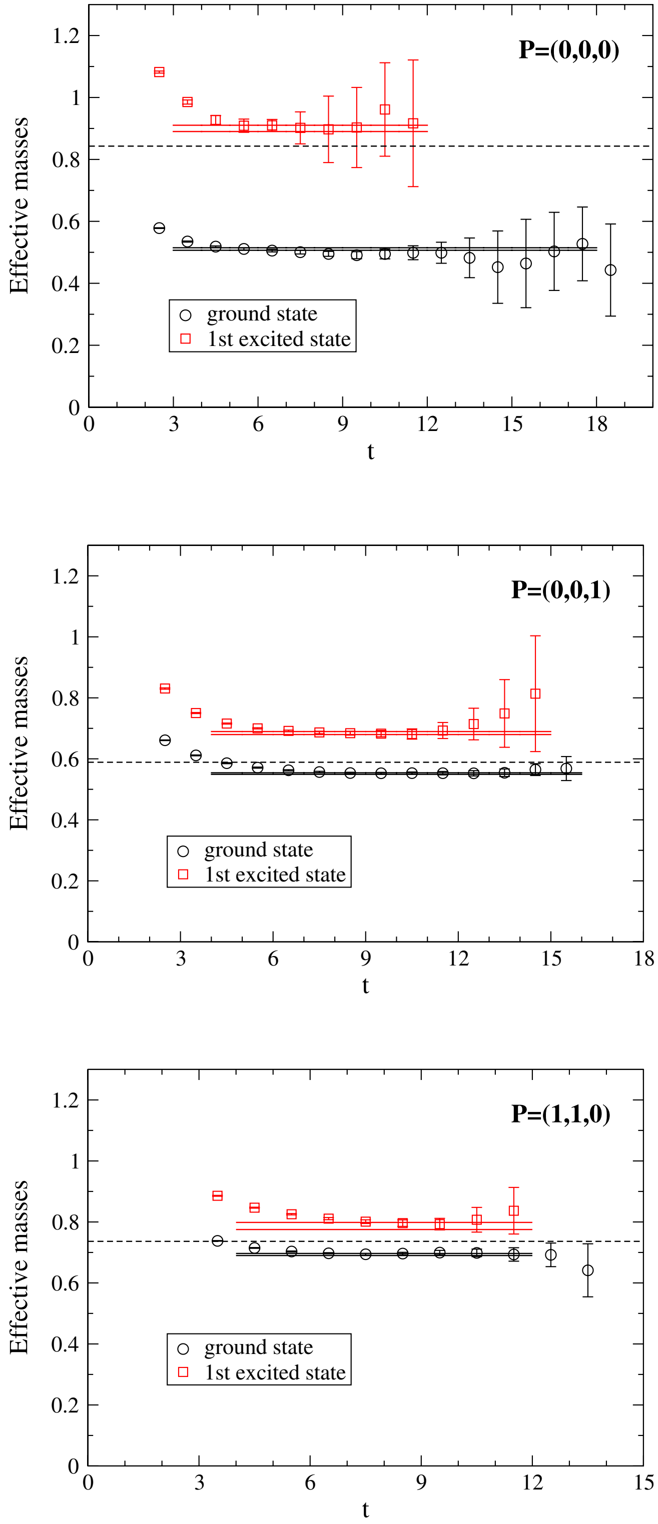

FIG. 5 (color online). The effective energies observed in the three momentum frames (0, 0, 0), (0, 0, 1), and (1, 1, 0), based on diagonalization of a correlation matrix with four or five operators, listed in Table III. The horizontal bands indicate the resulting energy levels derived from two-exponential fits to $\lambda_i(t)$, as discussed in the text. The dashed lines indicate the noninteracting two-pion levels as determined from the energies $E_{\rm lat}^{\rm d.r.}a$ in Table II.

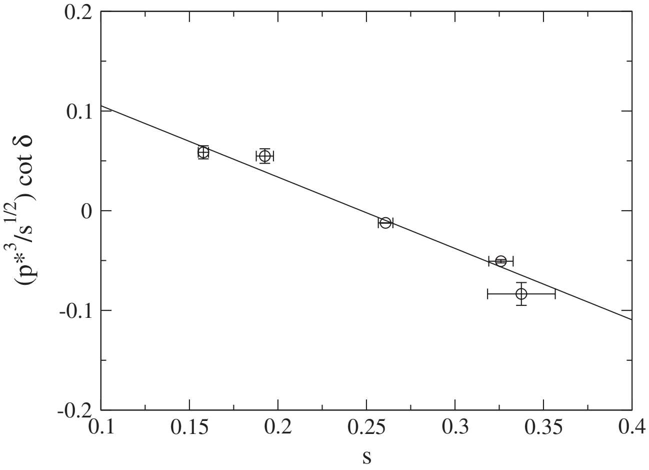

FIG. 6. Our data for $((ap^*)^3/\sqrt{sa^2})\cot\delta(s)$ as a function of sa^2, fitted to straight line behavior according to (40). The fit has $\chi^2/\text{d.o.f.} = 7.42/3$ and gives $g_{\rho\pi\pi} = 5.13(20)$ and $m_\rho a = 0.4972(42)$. The states $E_n(\mathbf{d})$ corresponding to various points can be deduced by the value of s in Table III. The plot data are shown in units of the lattice spacing.

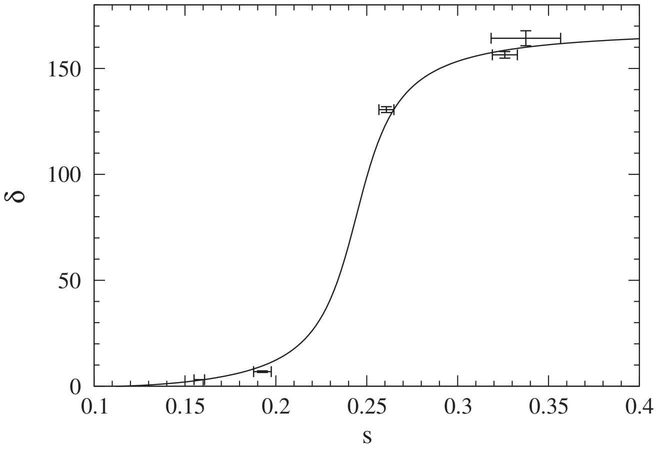

FIG. 7. The p-wave phase-shift values compared with the result from the fit to (40) in Fig. 6 for $g_{\rho\pi\pi} = 5.13$ and $m_\rho a = 0.4972$. The states $E_n(\mathbf{d})$ corresponding to various points can be deduced by the value of s in Table III.

$$g_{\rho\pi\pi}=5.13(20), \quad m_\rho a=0.4972(42), \quad m_\rho=792(7)(8)\,\text{MeV}. \tag{41}$$

Figure 7 exhibits the corresponding phase shift in the resonance region. The values (41) are obtained using the lattice dispersions relation (10). Given the systematic uncertainty with simulations on a single ensemble, they agree reasonably well with the results $g_{\rho\pi\pi} = 5.60(18)$ and $m_\rho a = 0.4833(41)$ obtained using the naive dispersion relation.

The value for the coupling (41) is near the experimental value $g_{\rho\pi\pi}^{\rm exp} \approx 5.97$. Our coupling is also compatible with the results in [10,12] within the errors given there. Note that [10,12] computed the coupling at larger pion mass.

In [13] a larger value $g_{\rho\pi\pi} = 6.77(67)$ and a substantially larger $m_\rho = 980$ MeV are observed at a similar pion mass $m_\pi = 290$ MeV. Our m_ρ is close to the prediction of the unitarized one-loop[4] ChPT, which leads to about $m_\rho \simeq 800$ MeV at $m_\pi \simeq 266$ MeV [50,51]. We also compared our $\delta(s)$ with the prediction of unitarized ChPT, recalculated for our $m_\pi = 266$ MeV by the authors of [52]: We find good agreement for $\sqrt{s} < m_\rho$ and reasonable agreement with one-loop results for $\sqrt{s} > m_\rho$.

Since the width is crucially influenced by the $\pi\pi$-phase space, this number derived for our pion mass comes out significantly smaller than the experimental value, so we present only $g_{\rho\pi\pi}$. This dimensionless coupling is expected to be almost independent of m_π [51], which was also explicitly verified in a study for several pion masses [13].

V. CONCLUSIONS AND OUTLOOK

Extracting scattering phase shifts and resonance properties is one of the most challenging problems in hadron spectroscopy based on lattice QCD. We combine several sophisticated tools to approach this problem: Lüscher's phase-shift relations for finite-volume lattices, moving frames, and variational analysis of correlation matrices, where a number of quark-antiquark and $\pi\pi$ interpolators with quantum numbers $I(J^{PC}) = 1(1^{--})$ are used. All needed contractions are evaluated using the distillation method with the Laplacian-Heaviside smearing of quarks. We find that these tools lead to precise values of the p-wave phase shift for $\pi\pi$ scattering at five values of pion relative momenta in the vicinity of the resonance. This allows a determination of the ρ resonance parameters m_ρ and Γ_ρ at our value of m_π.

The simulation is performed on an ensemble [29,30] of 280 gauge configurations with two mass-degenerate dynamical clover-improved Wilson fermions. The pion mass m_π is roughly 266 MeV, the lattice volume V is $16^3 \times 32$, and the spatial extent of the lattice is $L \simeq 1.98$ fm. The exponentially suppressed finite-volume corrections may not be completely negligible at our $m_\pi L \simeq 2.68$, and future simulations will have to improve on this. Larger lattices will necessitate stochastic estimation techniques to avoid the unsatisfactory scaling of full distillation with the lattice volume. Such a method has recently been provided in [18]. In the present study we calculated the quark propagation by calculating the distillation perambulators on all time slices, which is not very economical and only feasible in small volumes.

Along the way, we explore how well the lowest two energy levels can be obtained without the $\pi\pi$ interpolators in the variational basis. We also propose how to treat interpolators of different smearing widths in the same variational basis within the distillation method.

We demonstrate that a relatively accurate determination of the resonance parameters is possible with present-day techniques, within the limitation of small $m_\pi L$. For our pion mass we obtain the resonance mass $m_\rho = 792(7)(8)$ MeV and the $\rho \to \pi\pi$ coupling $g_{\rho\pi\pi} = 5.13(20)$, which is close to the experimental value $g^{\rm exp}_{\rho\pi\pi} \approx 5.97$. We prefer to give the coupling, since the actual width Γ_ρ is strongly affected by the phase space, which is small due to the large value of our pion mass.

Following the pion, the rho is the most prominent meson. With sharpened tools it is now becoming possible to analyze its decay properties. The present study of the ρ resonance gives us confidence that similar techniques can be applied to also extract the resonance parameters of some other hadronic resonances, and we intend to pursue research along these lines in the near future.

ACKNOWLEDGMENTS

First of all, we would like to kindly thank Anna Hasenfratz for providing the gauge configurations used for this work. We would like to thank Gilberto Colangelo, Georg Engel, Xu Feng, Christof Gattringer, Jose Pelaez, Akaki Rusetski, Igor Sega, Gerrit Schierholz, and Richard Woloshyn for valuable discussions. The calculations have been performed on the theory cluster at TRIUMF and on local clusters at the University of Graz and the University of Ljubljana. We thank these institutions for providing support. This work is supported by the Slovenian Research Agency, by the European RTN network FLAVIAnet (Contract No. MRTN-CT-035482), by the Slovenian-Austrian bilateral project (Contract No. BI-AT/09-10-012) and by the Natural Sciences and Engineering Research Council of Canada.

APPENDIX: CONTRACTIONS IN THE DISTILLATION METHOD

Here we provide the analytic expressions for correlators $C(t_f, t_i) = \langle \mathcal{O}_f(t_f)\mathcal{O}_i(t_i)\rangle$ that follow from general quark-antiquark interpolators with $|I, I_3\rangle = |1, 0\rangle$ [with examples given by $\mathcal{O}_{1-5}$ in (21)]

$$\mathcal{O}_f^{\bar{q}q}(t_f) = \frac{1}{\sqrt{2}}[\bar{u}_{s_f}(t_f)\Gamma_f^0\mathcal{F}_f^0(t_f, \mathbf{P})u_{s_f}(t_f) - \{u \leftrightarrow d\}],$$
$$\mathcal{O}_i^{\bar{q}q}(t_i) = \frac{1}{\sqrt{2}}[\bar{u}_{s_i}(t_i)\Gamma_i^0\mathcal{F}_i^0(t_i, -\mathbf{P})u_{s_i}(t_i) - \{u \leftrightarrow d\}], \quad \text{(A1)}$$

and general meson-meson (MM) interpolators with $|I, I_3\rangle = |1, 0\rangle$ [with examples given by $\mathcal{O}_6$ in (21)]

---

[4] The two-loop result strongly depends on a number of poorly known low energy constants, which are fixed in [51] also by using the lattice data on m_ρ, so the comparison to the two-loop result is not appropriate.

$$\begin{aligned}\mathcal{O}_f^{MM}(t_f) &= \frac{1}{\sqrt{2}}[\bar{d}_{s_f}(t_f)\Gamma_{1f}\mathcal{F}_f(t_f, \mathbf{p_{1f}})u_{s_f}(t_f)\bar{u}_{s_f}(t_f)\Gamma_{2f}\mathcal{F}_f(t_f, \mathbf{p_{2f}})d_{s_f}(t) - \{u \leftrightarrow d\}],\\ \mathcal{O}_i^{MM}(t_i) &= \frac{1}{\sqrt{2}}[\bar{u}_{s_i}(t_i)\Gamma_{1i}\mathcal{F}_i(t_i, -\mathbf{p_{1i}})d_{s_i}(t_i)\bar{d}_{s_i}(t_i)\Gamma_{2i}\mathcal{F}_i(t_i, -\mathbf{p_{2i}})u_{s_i}(t) - \{u \leftrightarrow d\}].\end{aligned} \tag{A2}$$

The subscripts $s_i, s_f = n, m, w$ denote the smearing width of the sink and source. The superscript "0" denotes that Γ^0 and $\mathcal{F}^0$ apply to $\bar{q}q$ interpolators, while Γ and $\mathcal{F}$ without superscripts apply to meson-meson interpolators.

The shape functions $\mathcal{F}$ (31) for our interpolators (21) are of three types:

$$\begin{aligned}\text{no}\,\nabla\text{:}\ \mathcal{F}^{c'c}_{\mathbf{x}'\mathbf{x}}(t,\mathbf{p}) &= \delta_{c'c}\delta_{\mathbf{x}'\mathbf{x}}\mathrm{e}^{\mathrm{i}\mathbf{p}\mathbf{x}},\\ \text{for}\,\nabla\text{:}\ \mathcal{F}^{c'c}_{\mathbf{x}'\mathbf{x}}(t,\mathbf{p}) &= \frac{1}{2}[\mathrm{e}^{\mathrm{i}\mathbf{p}\mathbf{x}}(\overrightarrow{\nabla}_j)^{c'c}_{\mathbf{x}'\mathbf{x}}(t) - (\overleftarrow{\nabla}_j)^{c'c}_{\mathbf{x}'\mathbf{x}}(t)\mathrm{e}^{\mathrm{i}\mathbf{p}\mathbf{x}}],\\ \text{for}\,\nabla\nabla\text{:}\ \mathcal{F}^{c'c}_{\mathbf{x}'\mathbf{x}}(t,\mathbf{p}) &= \sum_{j=1,2,3}(\overleftarrow{\nabla}_j)^{c'c_0}_{\mathbf{x}'x_0}(t)\mathrm{e}^{\mathrm{i}\mathbf{p}\mathbf{x}_0}(\overrightarrow{\nabla}_j)^{c_0c}_{\mathbf{x}_0\mathbf{x}}(t),\end{aligned} \tag{A3}$$

and we use the first choice (without ∇) within our meson-meson interpolators.

The contractions in Fig. 1 are expressed in terms of the perambulators τ (33), interpolator shape matrices ϕ (32), and Dirac matrices Γ, which are presented in Sec. II F of the main text. The analytic expressions for the contractions (A4)–(A7) below can be generally used for the interpolators of the form (A1) and (A2), or their cross correlators.

$$\langle \mathcal{O}_f^{\bar{q}q}(t_f)\mathcal{O}_i^{\bar{q}q}(t_i)\rangle = C^{\text{Fig. 1b}}(t_f, t_i) = -\mathrm{Tr}[\tau(t_i, t_f)\Gamma^0_f\phi(t_f, \mathcal{F}^0_f(\mathbf{P}))\tau(t_f, t_i)\Gamma^0_i\phi(t_i, \mathcal{F}^0_f(-\mathbf{P}))]. \tag{A4}$$

$$\begin{aligned}\langle \mathcal{O}_f^{MM}(t_f)O_i^{\bar{q}q}(t_i)\rangle = C^{\text{Fig. 1d}}(t_f, t_i) &= \mathrm{Tr}[\tau(t_i, t_f)\Gamma_{1f}\phi(t_f, (\mathbf{p_{1f}}))\tau(t_f, t_f)\Gamma_{2f}\phi(t_f, \mathcal{F}(\mathbf{p_{2f}}))\tau(t_f, t_i)\Gamma^0_i\phi(t_i, \mathcal{F}^0_i(-\mathbf{P}))]\\ &\quad - \{\mathbf{p_{1f}} \leftrightarrow \mathbf{p_{2f}}, \Gamma_{1f} \leftrightarrow \Gamma_{2f}\},\end{aligned} \tag{A5}$$

$$\begin{aligned}\langle \mathcal{O}_f^{\bar{q}q}(t_f)\mathcal{O}_i^{MM}(t_i)\rangle = C^{\text{Fig. 1e}}(t_f, t_i) &= -\mathrm{Tr}[\tau(t_f, t_i)\Gamma_{1i}\phi(t_i, \mathcal{F}(-\mathbf{p_{1i}}))\tau(t_i, t_i)\Gamma_{2i}\phi(t_i, \mathcal{F}(-\mathbf{p_{2i}}))\tau(t_i, t_f)\Gamma^0_f\phi(t_f, \mathcal{F}^0_f(\mathbf{P}))]\\ &\quad + \{\mathbf{p_{1i}} \leftrightarrow \mathbf{p_{2i}}, \Gamma_{1i} \leftrightarrow \Gamma_{2i}\},\end{aligned} \tag{A6}$$

$$\begin{aligned}\langle \mathcal{O}_f^{MM}(t_f)\mathcal{O}_i^{MM}(t_i)\rangle &= C^{\text{Fig. 1a}}_{\text{con}}(t_f, t_i) + C^{\text{Fig. 1c}}_{\text{dis}}(t_f, t_i).\\ C^{\text{Fig. 1a}}_{\text{con}}(t_f, t_i) &= \mathrm{Tr}[\tau(t_i, t_f)\Gamma_{1f}\phi(t_f, \mathcal{F}_f(\mathbf{p_{1f}}))\tau(t_f, t_i)\Gamma_{1i}\phi(t_i, \mathcal{F}_i(-\mathbf{p_{1i}}))]\\ &\quad \times \mathrm{Tr}[\tau(t_i, t_f)\Gamma_{2f}\phi(t_f, \mathcal{F}_f(\mathbf{p_{2f}}))\tau(t_f, t_i)\Gamma_{2i}\phi(t_i, \mathcal{F}_i(-\mathbf{p_{2i}}))] - \{\mathbf{p_{1i}} \leftrightarrow \mathbf{p_{2i}}, \Gamma_{1i} \leftrightarrow \Gamma_{2i}\},\\ C^{\text{Fig. 1c}}_{\text{dis}}(t_f, t_i) &= \mathrm{Tr}[\tau(t_i, t_f)\Gamma_{2f}\phi(t_f, \mathcal{F}_f(\mathbf{p_{2f}}))\tau(t_f, t_f)\Gamma_{1f}\phi(t_f, \mathcal{F}_f(\mathbf{p_{1f}}))\tau(t_f, t_i)\Gamma_{2i}\phi(t_i, \mathcal{F}_i(-\mathbf{p_{2i}}))\tau(t_i, t_i)\\ &\quad \times \Gamma_{1i}\phi(t_i, \mathcal{F}_i(-\mathbf{p_{1i}}))] + \mathrm{Tr}[\tau(t_i, t_f)\Gamma_{1f}\phi(t_f, \mathcal{F}_f(\mathbf{p_{1f}}))\tau(t_f, t_f)\Gamma_{2f}\phi(t_f, \mathcal{F}_f(\mathbf{p_{2f}}))\tau(t_f, t_i)\\ &\quad \times \Gamma_{1i}\phi(t_i, \mathcal{F}_i(-\mathbf{p_{1i}}))\tau(t_i, t_i)\Gamma_{2i}\phi(t_i, \mathcal{F}_i(-\mathbf{p_{2i}}))] - \{\mathbf{p_{1i}} \leftrightarrow \mathbf{p_{2i}}, \Gamma_{1i} \leftrightarrow \Gamma_{2i}\}.\end{aligned} \tag{A7}$$

[1] K. Nakamura *et al.*, J. Phys. G **37**, 075021 (2010).
[2] M. Lüscher, Commun. Math. Phys. **105**, 153 (1986).
[3] M. Lüscher, Nucl. Phys. **B354**, 531 (1991).
[4] M. Lüscher, Nucl. Phys. **B364**, 237 (1991).
[5] C. R. Gattringer and C. B. Lang, Nucl. Phys. **B391**, 463 (1993).
[6] M. Göckeler, H. Kastrup, J. Westphalen, and F. Zimmermann, Nucl. Phys. **B425**, 413 (1994).
[7] K. Rummukainen and S. Gottlieb, Nucl. Phys. **B450**, 397 (1995).
[8] C. Kim, C. T. Sachrajda, and S. R. Sharpe, Nucl. Phys. **B727**, 218 (2005).
[9] X. Feng, K. Jansen, and D. B. Renner, Proc. Sci., LAT2010 (2010) 104.
[10] S. Aoki, M. Fukugita, K.-I. Ishikawa, N. Ishizuka, K. Kanaya, Y. Kuramashi, Y. Namekawa, M. Okawa, K. Sasaki, A. Ukawa, and T. Yoshi (CP-PACS Collaboration), Phys. Rev. D **76**, 094506 (2007).
[11] M. Göckeler, R. Horsley, Y. Nakamura, D. Pleiter, P. E. L. Rakow, G. Schierholz, and J. Zanotti (QCDSF Collaboration), Proc. Sci., LAT2008 (2008) 136 [arXiv:0810.5337].
[12] S. Aoki, K. I. Ishikawa, N. Ishizuka, K. Kanaya, Y. Kuramashi, Y. Namekawa, M. Okawa, Y. Taniguchi, A.

Ukawa, N. Ukita, T. Yamazaki, and T. Yoshié (PACS-CS Collaboration), Proc. Sci., LATTICE2010 (2010) 108 [arXiv:1011.1063].

[13] X. Feng, K. Jansen, and D. B. Renner, Phys. Rev. D **83**, 094505 (2011).

[14] J. Frison, S. Durr, Z. Fodor, C. Hoelbling, S. Katz, S. Krieg, T. Kurth, L. Lellouch, T. Lippert, A. Portelli, A. Ramos, and K. K. Szabo (BMW Collaboration), Proc. Sci., LATTICE2010 (2010) 139 [arXiv:1011.3413].

[15] C. McNeile and C. Michael, Phys. Lett. B **556**, 177 (2003).

[16] G. P. Engel, C. B. Lang, M. Limmer, D. Mohler, and A. Schäfer (BGR [Bern-Graz-Regensburg] Collaboration), Phys. Rev. D **82**, 034505 (2010).

[17] J. Bulava *et al.*, Phys. Rev. D **82**, 014507 (2010).

[18] C. Morningstar, J. Bulava, J. Foley, K. J. Juge, D. Lenkner, M. Peardon, and C. H. Wong, Phys. Rev. D **83**, 114505 (2011).

[19] J. J. Dudek, R. G. Edwards, M. J. Peardon, D. G. Richards, and C. E. Thomas, Phys. Rev. D **82**, 034508 (2010).

[20] M. Peardon, J. Bulava, J. Foley, C. Morningstar, J. Dudek, R. G. Edwards, B. Joo, H.-W. Lin, D. G. Richards, and K. J. Juge (Hadron Spectrum Collaboration), Phys. Rev. D **80**, 054506 (2009).

[21] J. J. Dudek, R. G. Edwards, M. J. Peardon, D. G. Richards, and C. E. Thomas, Phys. Rev. Lett. **103**, 262001 (2009).

[22] J. J. Dudek, R. G. Edwards, M. J. Peardon, D. G. Richards, and C. E. Thomas, Phys. Rev. D **83**, 071504 (2011).

[23] J. J. Dudek, R. G. Edwards, B. Joo, M. J. Peardon, D. G. Richards, and C. E. Thomas, Phys. Rev. D **83**, 111502 (2011).

[24] R. G. Edwards, J. J. Dudek, D. G. Richards, and S. J. Wallace, arXiv:1104.5152.

[25] C. Michael, Nucl. Phys. **B259**, 58 (1985).

[26] M. Lüscher, Commun. Math. Phys. **104**, 177 (1986).

[27] M. Lüscher and U. Wolff, Nucl. Phys. **B339**, 222 (1990).

[28] B. Blossier, M. DellaMorte, G. von Hippel, T. Mendes, and R. Sommer, J. High Energy Phys. 04 (2009) 094.

[29] A. Hasenfratz, R. Hoffmann, and S. Schaefer, Phys. Rev. D **78**, 054511 (2008).

[30] A. Hasenfratz, R. Hoffmann, and S. Schaefer, Phys. Rev. D **78**, 014515 (2008).

[31] V. Bernard, M. Lage, U.-G. Meißner, and A. Rusetsky, J. High Energy Phys. 08 (2008) 024.

[32] P. Giudice, D. McManus, and M. Peardon, Proc. Sci., LAT2010 (2010) 105 [arXiv:1009.6192].

[33] U. G. Meißner, K. Polejaeva, and A. Rusetsky, Nucl. Phys. **B846**, 1 (2011).

[34] C. Gattringer, L. Y. Glozman, C. B. Lang, D. Mohler, and S. Prelovsek, Phys. Rev. D **78**, 034501 (2008).

[35] S. Prelovsek and D. Mohler, Phys. Rev. D **79**, 014503 (2009).

[36] W. Detmold, K. Orginos, M. J. Savage, and A. Walker-Loud, Phys. Rev. D **78**, 054514 (2008).

[37] C. Gattringer, C. Hagen, C. B. Lang, M. Limmer, D. Mohler, and A. Schäfer, Phys. Rev. D **79**, 054501 (2009).

[38] S. Sasaki, T. Blum, and S. Ohta, Phys. Rev. D **65**, 074503 (2002).

[39] A. Hasenfratz, R. Hoffmann, and S. Schaefer, J. High Energy Phys. 05 (2007) 029.

[40] A. Stathopoulos and J. R. McCombs, ACM Trans. Math. Softw. **37**, 21:1 (2010).

[41] M. Lüscher, J. High Energy Phys. 07 (2007) 081.

[42] M. Lüscher, J. High Energy Phys. 12 (2007) 011.

[43] D. Toussaint and W. Freeman, arXiv:0808.2211.

[44] R. Sommer, Nucl. Phys. **B411**, 839 (1994).

[45] A. Hasenfratz and F. Knechtli, Phys. Rev. D **64**, 034504 (2001).

[46] A. Hasenfratz, R. Hoffmann, and F. Knechtli, Nucl. Phys. B, Proc. Suppl. **106–107**, 418 (2002).

[47] C. Gattringer, R. Hoffmann, and S. Schaefer, Phys. Rev. D **65**, 094503 (2002).

[48] L. S. Brown and R. L. Goble, Phys. Rev. Lett. **20**, 346 (1968).

[49] F. Renard, Nucl. Phys. **B82**, 1 (1974).

[50] C. Hanhart, J. R. Pelaez, and G. Rios, Phys. Rev. Lett. **100**, 152001 (2008).

[51] J. R. Pelaez and G. Rios, Phys. Rev. D **82**, 114002 (2010).

[52] J. Nebreda, J. R. Pelaez, and G. Rios, Phys. Rev. D **83**, 094011 (2011).